# Deep learning methods for blood flow reconstruction in a vessel with contrast enhanced x-ray computed tomography

Shusong Huang, Monica Sigovan, Bruno Sixou

Received: Added at production | Revised: Added at production | Accepted: Added at production

DOI: xxx/xxxx

ARTICLE TYPE

# Deep learning methods for blood flow reconstruction in a vessel with contrast enhanced X-ray CT.

Huang Shusong | Sigovan Monica | Sixou Bruno*

[1]CREATIS, CNRS UMR5220; Inserm U630; INSA-Lyon; Université Lyon 1; Université de Lyon, F-69621 Villeurbanne Cedex, France.

**Correspondence**
Email: bruno.sixou@insa-lyon.fr

**Summary**

The reconstruction of blood velocity in a vessel from contrast enhanced X-ray CT projections is a complex inverse problem. It can be formulated as reconstruction problem with a partial differential equation constraint. A solution can be estimated with the a variational adjoint method and proper orthogonal decomposition basis. In this work, we investigate new inversion approaches based on proper orthogonal decompositions coupled with deep learning methods. The effectiveness of the reconstruction methods is shown with simulated realistic stationary blood flows in a vessel. The methods outperform the reduced adjoint method and show large speed-up at the online stage.

**KEYWORDS:**
Tomography, inverse problems, hemodynamics, proper orthogonal decomposition(POD)

## 1 | INTRODUCTION

The study of blood flow is crucial for the treatment of cardiovascular diseases [1,2,3] but it remains a difficult task. There are non-invasive quantitative imaging methods of intravascular hemodynamics. A low spatiotemporal resolution is obtained with imaging modalities like magnetic resonance and ultrasound [4,5,6,7] and some hemodyamic parameters cannot be calculated accurately. X-ray CT have been much less investigated [8,9,10,11,12]. The proposed methods rely often on the evolution of the tracer concentration gradients. Recently, we have studied a new reconstruction approach for the velocity field in a vessel with contrast enhanced spectral CT [13]. The Radon projections are measured perpendicularly to the vessel axis. A transport partial differential equation is used to model the propagation of the tracer injected in the inlet. Simulations experiments have shown that the velocity field can be estimated with a good resolution with the adjoint method [14,15] but the computational time remains too high. In order to reduce the compational costs of the adjoint method, we have also investigated reduced-order modeling based on Proper Orthogonal Decomposition (POD) [16]. The principle of the method is to represent the velocity field, the Radon projections and the adjoint variable in terms of known basis functions that capture the more important information. The governing equations of the adjoint method are then projected onto the linear subspaces estimated with this principal component analysis. A large reduction of the computation time is obtained in comparison with high-fidelity simulations and the dominant flow patterns are identified. Yet, the method is still time consuming since we have to evaluate repeatedly the ouput of forward and adjoint partial differential equations to solve the inverse problem. Moreover, the structure of the physical problem and the governing equations for the diffusion of the tracer must be known precisely.

On the other hand, novel methodologies based on deep learning have been proposed recently to solve complex inverse problems [17]. There are many situations in which data are abundant but governing laws are uncertain or do not exist. The use of deep learning models is particularly promising in scientific problems involving processes that are not completely understood, or where it is computationally infeasible to run models at high resolutions in space and time. Deep learning structures are often used as a

surrogate model where the goal is to accurately reproduce the behavior of model at substantially reduced computational cost. For complex scientific and engineering applications, deep learning alone can not be considered sufficient. Many hybrid physics-deep learning frameworks have been studied, that integrate traditional physics-based modeling approaches with state-of-the-art machine learning or deep learning technique [18,19]. Several methods incorporate physical knowledge into loss functions to help deep learning models to capture patterns consistent with physical laws. They thus considered physics-guided loss functions where the governing equations are used as regularizers to reduce the search space of parameters [20,21,22,23]. In several works, a neural network is used to approximate the solution operator mapping elements of the space of the parameters of a Partial Differential Equation (PDE) and the space of the solutions of this PDE by minimizing a loss functional using the discretized values of the solution and of the parameters. These approaches may be successful but are not robust to mesh refinement. In order to overcome some limitations of these works, there has been some work about operator approximations with deep learning techniques that have the property of discretization invariance. These neural networks are defined to act between infinite-dimensional function spaces. PCA-Net uses neural networks to map between PCA coefficients representing input and output functions [24,25]. Recently, DeepONet have been investigated for operator approximation comprising two sub-networks, the branch and trunk network [26,27]. In [28], the authors couples a POD with a convolutional network to solve the cardiac electrophysiology inverse problem.

In this work, inspired by these approaches and in order to improve the reconstruction results obtained for blood velocity reconstruction with our POD-adjoint approach, we investigate the coupling of POD model reduction with deep learning techniques. We compare several neural network architectures to approximate the inverse operator. The quantitites of interest, the velocity field and Radon projections, corresponding to the inputs and the outputs of our inverse problem are expanded in terms of appropriate sets of basis functions obtained from snapshots. Various neural network architectures are used to map the coefficient associated to the representations of these functions. The efficiency of the framework is demonstrated with numerical examples with stationary velocity fields with realistic simulations.

The paper is organized as follows. After the introduction, in section 2, the inverse problem will be presented and the variational inversion methodology based on POD will be summarized. Then the deep learning approaches studied to approximate the unknown velocity field are described in detail. In section 4, the simulation results achieved with these methods to solve the inverse problem are detailed and discussed.

## 2 | THEORETICAL FRAMEWORK

### 2.1 | Inverse problem formulation and adjoint method with POD reduction

The inverse problem formulation for parametrically varying conditions has been presented in detail in [16]. In this section, we summarize here the set up and the adjoint method based on Proper Orthogonal Decomposition. A set of model parameters $\boldsymbol{\mu}$ in the set $\mathcal{M}$ is used to parametrize the inverse problem. Two-dimensional Radon projections are acquired perpendicularly to the $z$ axis which is the main vessel axis and flow direction. We denote $Q = \Omega \times [0, T]$ the space-time box where $\Omega$ is a bounded spatial domain and $[0, T]$ the time interval. A convection-diffusion equation is used to model the propagation of the contrast agent in the vessel with the velocity field $\mathbf{V} = (u, v, w) : [0, T] \times \Omega \to \mathbb{R}^3$ obtained with the Navier-Stokes (NS) equations [13] which depends on the first subset $\boldsymbol{\mu}_1$ of $\boldsymbol{\mu}$ related to the boundary and initial conditions. The contrast agent enters the vessel through a disk ($\mathcal{D}$) in the plane $z = 0$. The transport equation of the tracer concentration $f(\mathbf{x}, t)$ with initial and boundary conditions is written as follows:

$$\begin{cases} e(f, \mathbf{V}, \mu) = \frac{\partial f(\mathbf{x},t)}{\partial t} + \mathbf{V} \cdot \nabla f(\mathbf{x}, t) - D \triangle f(\mathbf{x}, t) = 0 \\ f(\mathbf{x}, t) = f_{in} \quad \forall x \in (\mathcal{D}) \ \ \forall t \in [0, T] \\ f(\mathbf{x}, 0) = 0 \quad \forall x \in \Omega - (\mathcal{D}) \end{cases} \tag{1}$$

where the convective term is given by:

$$\mathbf{V} \cdot \nabla f(\mathbf{x}, t) = u \frac{\partial f(\mathbf{x}, t)}{\partial x} + v \frac{\partial f(\mathbf{x}, t)}{\partial y} + w \frac{\partial f(\mathbf{x}, t)}{\partial z} \tag{2}$$

The inlet concentration of the tracer $f_{in}$ and the diffusion coefficient $D$ that are used to parametrize the transport equation correspond to the second subset $\boldsymbol{\mu}_2$ of the model parameters $\boldsymbol{\mu}$ . The density of the other materials is neglected and the evolution of the Radon projections with time is related to tracer concentration. Let $\Sigma \in \mathbb{R}^2$ be a bounded Lipschitz domain, the Radon

transform of the concentration of the tracer can be written as:

$$Rf(\theta, s) = \int\limits_{\Sigma \cap L_r(\theta,s)} f(\mathbf{x}) dl(\mathbf{x}) \tag{3}$$

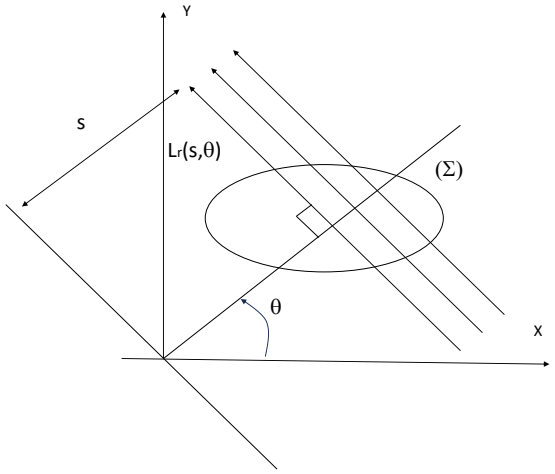


**Figure 1** Principle of integral Radon transform.

The line $L_r(\theta, s)$ is determined by the angle $\theta \in [0, \pi]$ and by the distance $s \in [-a, a]$ from the origin as displayed on Figure 1 [29]. The scanner is rotating with time and the Radon projections are acquired for $N_\theta$ projection angles regularly distributed in the angular range $\Delta\theta(t)$. For each angle, $N_p$ projections are measured and the 2D Radon projections are obtained for $N_z$ values along the z axis, with $z \in [0, z_{max}]$.

Our aim is to estimate the velocity $\mathbf{V}(\mathbf{x}, t)$ from the linear equations $Rf(\theta, s, z) = p^\delta(\theta, s, z)$, where $p^\delta$ are the noisy projections, $s$ and $z$ are coordinates of the two-dimensional detector. In the framework of the adjoint method, the inverse problem is formulated as a constrained minimization problem with the Lagrangian $L_a$ obtained with a dual variables $h : [0, T] \rightarrow L_2(\Omega)$ and written as:

$$L_a(f, \mathbf{V}, h, \boldsymbol{\mu}) = J(f, \mathbf{V}, \boldsymbol{\mu}) + \beta \int\limits_0^T < e(f, \mathbf{V}, \boldsymbol{\mu}), h(t) > dt \tag{4}$$

where $\beta$ is a Lagrangian parameter and $< ., . >$ denotes the $L_2(\Omega)$ scalar product. The cost functional J can be written as:

$$J(f, \mathbf{V}, \boldsymbol{\mu}) = \frac{1}{2} \int_0^T \|Rf(\theta, s, z) - p^\delta(t)\|_2^2 dt + \frac{\alpha_s}{2} \||\nabla \mathbf{V}|\|_2^2 \tag{5}$$

with $\boldsymbol{\mu} = (\boldsymbol{\mu_1}, \boldsymbol{\mu_2})$ and $\alpha_s$ a regularization parameter [16]. The system of PDE equation used in the adjoint method is based on the optimality conditions for the Lagrangian [13]. The adjoint method with the POD reduced approach is based on the assumption that the solution manifold $\{f(\boldsymbol{\mu}), \mathbf{V}(\boldsymbol{\mu}), h(\boldsymbol{\mu}); \boldsymbol{\mu} \in \mathcal{M}\}$ can be approximated by a low dimensional subspace in an offline phase by the snapshots, $\{f(\boldsymbol{\mu}), \mathbf{V}(\boldsymbol{\mu}), h(\boldsymbol{\mu}); \boldsymbol{\mu} \in \mathcal{M}_s\}$ where $\mathcal{M}_s$ is a discrete subset of parameters $\mathcal{M}_s \subset \mathcal{M}$. The snapshots are projected on low dimensional spaces to obtain the reduced basis $(\Psi_{f,i})_{1 \leq i \leq N_f}$, $(\boldsymbol{\Psi}_{V,j})_{1 \leq j \leq N_v}$, $(\Psi_{h,k})_{1 \leq k \leq N_h}$ with dimensions $N_f$, $N_V^3$ and $N_h$. The offline step consists in building these POD basis for the tracer concentration, velocity and adjoint variables. For the tracer concentration, the POD basis vectors are obtained with the minimization of the projection error:

$$\frac{1}{N_s} \sum_{\boldsymbol{\mu} \in \mathcal{M}_s} \|f(\boldsymbol{\mu}) - \Pi_{\Psi_f} f(\boldsymbol{\mu})\|^2_{L_2(\Omega \times [0,T])} \tag{6}$$

where $N_s$ is the total number of snapshots, $\Pi_{\Psi_f}$ denotes the projection on the reduced finite dimensional space spanned by the basis $(\Psi_{f,i})_{1 \leq i \leq N_f}$. Similar error metrics are used for the adjoint variable and the velocity field.

During the online phase, for a test value of $\boldsymbol{\mu}$, $f(\boldsymbol{\mu}), \mathbf{V}(\boldsymbol{\mu}), p(\boldsymbol{\mu})$ are projected onto the reduced subspaces. A system of low dimensional ordinary differential equations is thus obtained. The PDE constraint $e(f, \mathbf{V}, \boldsymbol{\mu}) = 0$ can then be formulated as

$\frac{d\hat{f}}{dt} = \hat{A}\hat{f}$ with $f = \Psi_f \hat{f}$, and $\hat{f}$ the reduced coefficients for the tracer concentration and $\hat{A} = \Psi_f^t A \Psi_f$ the reduced operator corresponding to the transport equation. The model reductions applied to adjoint equation and to the gradient of the functional are detailed in [13]. This approach is still very time consuming and we will present new deep learning methods.

## 2.2 | Inverse problem formulation with deep learning approaches

The approaches studied in this work combine model reduction with deep neural networks to learn the mapping between two Hilbert spaces, $\mathcal{L}_V = L_2(\Omega \to \mathbb{R}^3)$ for the velocity field $\mathbf{V}$ and $\mathcal{L}_p = L_2([0,T] \times [-a,a] \times \left[0, z_{max}\right] \to \mathbb{R})$ for the Radon projections $p$. We consider only stationary velocity fields but we have to include the time domain to describe the evolution of the tracer density and of the Radon projections. In the following, the POD for the Radon projections includes the time domain.

The velocity space $\mathcal{L}_V$ is considered as the product of three spaces $\mathcal{L}_V = \mathcal{L}_V^x \times \mathcal{L}_V^y \times \mathcal{L}_V^z$ of three spaces corresponding to the components of the velocity field. We have $\mathcal{L}_V^x = \{V_x : \Omega \to \mathbb{R}\}$ for the velocity component along $x$ and similar definitions hold for the other directions. Our aim is to determine a nonlinear inverse operator $\Psi = \Psi^x \times \Psi^y \times \Psi^z : \mathcal{L}_p \to \mathcal{L}_V$ from samples corresponding to the two probability measures on these spaces, the probability measures $\nu$ on $\mathcal{L}_p$ and its pushforward measure $\Psi^*\nu$ on $\mathcal{L}_V$. With these notations, for given Radon projections $p$, the velocity component are given by $V_x = \Psi^x(p)$, $V_y = \Psi^y(p)$ and $V_z = \Psi^z(p)$. This operator is approximated with a class of parametric operators $\Psi_\theta = \Psi_\theta^x \times \Psi_\theta^y \times \Psi_\theta^z : \mathcal{L}_p \to \mathcal{L}_V$ with different neural network architectures, where $\theta \in \mathbb{R}^D$ denotes the set of the $D$ neural network parameters. This corresponds to an inverse nonlinear operator learning. The direct learning of solution operators of inverse problems is currently a popular research area, and many deep neural networks architectures have been proposed [17]. One difficulty is the interplay between the ill-posedness of the learning and ill-posedness of the inverse problem itself. In practice, a finite number $N$ of samples for the Radon projections and velocity measures are available $\{p_n\}_{1\le n\le N}$ and $\{V_n = \Psi(p_n)\}_{1\le n\le N}$ defining empirical measures. To determine the optimal parameter $\theta^*$,we will use the cost function $\mathcal{L}$:

$$\mathcal{L} = \frac{1}{N}\sum_{n=1}^{N} \frac{E_n^x + E_n^y + E_n^z}{\|\Psi^x(p_n)\|_2 + \|\Psi^y(p_n)\|_2 + \|\Psi^z(p_n)\|_2} \tag{7}$$

where $E_n^x = \|\Psi^x(p_n) - \Psi_\theta^x(p_n,\theta)\|_{L_2}^2 = \|V_x(p_n) - \Psi_\theta^x(p_n,\theta)\|_{L_2}^2$ is the reconstruction error along $x$ and similar definitions hold for the other axes. In practice, in view of the non-convex nature of the optimization over $\theta$ , we may only have access to an approximation of $\theta^*$.

In this work, we have used approaches similar to the ones presented in [25,28]. In order to learn a data-driven mapping between the two Hilbert spaces, we first estimate finite dimensional approximations of these spaces with POD. We approximate the identity mappings $I_{\mathcal{L}_p}$ and $I_{\mathcal{L}_V}$ by the composition of two maps, a linear encoder and a linear decoder, with finite-dimensional range and domain respectively. The finite-dimensional outputs of the encoders are called latent codes corresponding to the POD coefficients and we will build a mapping $\alpha$ between these latent codes. In the following, we will denote $F_{\mathcal{L}_p}$ and $G_{\mathcal{L}_p}$ the encoder and the decoder of the space $\mathcal{L}_p$. Similarly, we will denote $F_{\mathcal{L}_V}$ and $G_{\mathcal{L}_V}$ the encoder and the decoder of the space $\mathcal{L}_V$. To summarize we have the following approximations, $I_{\mathcal{L}_p} \simeq G_{\mathcal{L}_p} \circ F_{\mathcal{L}_p}$, $I_{\mathcal{L}_V} \simeq G_{\mathcal{L}_V} \circ F_{\mathcal{L}_V}$; $\Psi_\theta \simeq G_{\mathcal{L}_V} \circ \alpha \circ F_{\mathcal{L}_p}$. The combination of POD with a neural network is the basis of the computational methodology.

In the framework of the deep learning approaches, the dimension reduction is not performed on the density, the adjoint variable and the velocity field as in the adjoint method, but on the Radon projections and the velocity field. We will denote $N_R$ and $N_V^3$ the number of basis elements for the Radon projections and the velocity field respectively. It should be noted that the POD could be replaced by encoding/decoding with nonlinear auto-encoders. The first step thus consists to obtain finite dimensional approximations on the velocity and Radon projection spaces. The POD presented above lead to orthonormal bases $\{\psi_{Rf,i}\}_{1\le i\le N_R}$ pour $\mathcal{L}_p$ and $\{\psi_{V,i}\}_{1\le i\le N_V} \times \{\psi_{V,i}^x\}_{1\le i\le N_V} \times \{\psi_{V,i}^y\}_{1\le i\le N_V} \times \{\psi_{V,i}^z\}_{1\le i\le N_V}$ for $\mathcal{L}_V$ which are truncated to the first $N_R$ et $N_V$ first modes before the training of the network.

a) POD-FC method

The first approach presented in this section is similar to the work presented in [25,24] to achieve modeling of nonlinear operators. The method is based on a fully connected network (FC) and it will be called POD-FC in the following. Given Radon projetions $p \in \mathcal{L}_p$, the operator $\Psi_\theta$ is defined for the $x$ component with:

$$\Psi_\theta^x(p,\theta)(M) = \sum_{j=1}^{N_V} \alpha_j^x(F_{\mathcal{L}_p}p,\theta)\psi_{V,j}^x(M) \tag{8}$$

for $M \in \Omega$ for stationary velocity fields. The function $\alpha_j^x : \mathbb{R}^{N_R} \times \mathbb{R}^D \to \mathbb{R}$, for $1 \leq j \leq N_V$, is mapping the coefficients obtained for the POD of $p$ , $F_{\mathcal{L}_p} p = \{(\psi_{Rf,i}, p)\}_{1 \leq i \leq N_R}$ and the coefficients corresponding to the velocity field along $x$, $F^x_{\mathcal{L}_V} V$ . The others definitions are similar for the other axes.

b) POD-CNN method

The second neural network architecture studied is based on a Convolutional Neural Network (CNN) $\alpha$ and it will be called POD-CNN. It leverages some ideas presented in [28]. In this work, the authors proposed a slightly different architecture, for cardiac electrophysiology inverse problems, leading to an approximation of the mapping between the input surface potentials and the epicardial potential field. The predicted solutions is also consistent with the problem physics, approximated by means of PDEs and the approach is also an instance of physics informed deep learning model, that exploits physical laws to improve the predictive power of the model. By resorting to reduced order modeling techniques, they managed to mitigate the effects of the ill-posedness of the inverse problem with a dimensionality reduction of the solution space. The network learns a latent reduced representation of the epicardial potential field and an data-driven approximate version of the inverse operator. This latent representation corresponds to the the coefficients arising from the projection of the epicardial potential field onto a spatio-temporal reduced subspace. The space of admissible solutions for the inverse problem is further shrinked, as additional physical constraints have been added, and it ultimately reduces to a low-dimensional and physically consistent manifold. For our inverse problem, the corresponding approximate inverse operator can be written for the $x$ component as:

$$\Psi^x_\theta(p, \theta)(M) = \sum_{j=1}^{N_V} \alpha_j^x(p, \theta)\psi^x_{V,j}(M) \tag{9}$$

with similar defintions for $y$ and $z$. It should be noted that the operator $F_{\mathcal{L}_p}$ and the Proper Orthogonal Decomposition in the input space are not used. The two architectures will be tested in the next section with numerical experiments.

## 3 | NUMERICAL EXPERIMENTS

In this section, we detail some numerical experiments to test the deep learning approaches on a realistic numerical phantom with complex flows described by Navier-Stokes equations. We will focuss here on stationary velocity fields. In order to train the neural networks, we have to first to build POD basis for the velocity field for the POD-CNN method and the bases for the Radon projections and the velocity for the POD-FC method. We summarize the finite elements simulation and POD bases construction. They are detailed in [13,16]. Then we present the neural network architectures and training methodology.

### 3.1 | Finite elements simulation details, POD bases construction and data generation

The vessel used for the simulations is displayed in Figure 2. Steady-state Navier-Stokes equation have been used to simulate realistic velocity fields to be reconstructed $\mathbf{V}^*(\mathbf{x})$ [13]. The velocity fields are used in the transport equation (Eq.1) to estimate the tracer concentration and the Radon projections. The finite elements simulations have been performed with the Fenics software [30,31]. For time domain, we have used $[0, T] = [0s, 0.5s]$, with $N_t = 10$ steps and a time step $dt = 0.01s$ for Euler explicit time discretization [32]. Longer simulations gives similar reconstruction errors and results for the comparison between the methods. The spatial domain is discretized with $P1$ finite elements and 56845 nodes. For the simulation of the Navier-Stokes equation, Taylor-Hood ($P2 - P1$) finite elements have been used [33,34,35]. The Navier-Stokes have been simulated with the Incremental Pressure Correction scheme in Fenics [30,31]. Regularly spaced Radon projections perpendicular to the vessel direction are calculated with the Scipy python library [36] for $N_z = 100$ values. They are estimated for $N_{proj} = 285$ values, for $N_\theta = 30$ projection angles in the angular range $\Delta\theta = 180°$ for each time step. A Gaussian white noise with peak-to-peak signal-to-noise ratio (PPSNR) between 0 and 20 dB is used to corrupt the projections, which is defined as:

$$PPSNR = 20log(\frac{S_{max}}{n_{max}}) \tag{10}$$

where $S_{max}$ is the maximum signal amplitude and $n_{max}$ the maximum noise amplitude. The snapshots for the Radon projection distribution are sampled both in time and parameter space with a a regular grid sampling. For the velocity, they are only sampled in parameter space. The first subset $\boldsymbol{\mu_1}$ of the model parameters $\boldsymbol{\mu} = (\boldsymbol{\mu_1}, \boldsymbol{\mu_2})$ is related to the initial/boundary conditions for the

**Figure 2** The finite element mesh used for the simulations.

.

velocity field. The NS equation in an incompressible viscous flow is:

$$\begin{cases} \mathbf{V}.\nabla\mathbf{V} + \nabla p - \nu \triangle \mathbf{V} = 0 \\ \nabla.\mathbf{V} = 0 \\ \mathbf{V} = \mathbf{V}_{\partial\Omega} \ \ on \ \ \partial\Omega \end{cases} \tag{11}$$

where $\nu$ is the kinematic viscosity, $p(\mathbf{x})$ the pressure field and $\mathbf{V}_{\partial\Omega}$ the velocity field on the boundary $\partial\Omega$. The time derivative of the velocity is cancelled for the steady-state equation. The boundary $\partial\Omega = \Gamma_{in} \cup \Gamma_{out} \cup \Gamma_s$ of the spatial domain $\Omega$ consists of an inflow part $\Gamma_{in}$ on the plane $z = 0$, of an outflow boundary $\Gamma_{out}$ on the output plane and of the lateral side of the vessel $\Gamma_s$. A parabolic profile is used in the inlet boundary with a maximum value in the middle of this region denoted as $\mathbf{V}_{\Gamma_{in},max}$. We assume that the velocity on the boundary $\Gamma_s$ vanishes. For the oulet, we use $\nu\partial_{\mathbf{N}}\mathbf{V} + p\mathbf{N} = 0$ where $\mathbf{N}$ is the unit normal vector and $\partial_{\mathbf{N}}$ the normal derivative .

The stationary velocity fields will be parametrized with $\mu_1 = (\mathbf{V}_{\Gamma_{in},max}, p_{\Gamma_{out}})$, where $p_{\Gamma_{out}}$ is the pressure on the outflow part. This parameter is sampled regularly for inlet velocities between 0.02 and 0.6 m/s and for output pressures between 0 and 1000 Pa. The largest outlet of the vessel has a diameter which is 1.5 larger than the one of the small outlet and as a first approximation, the same outlet pressure is used for both.

The POD basis for the Radon projections are obtained from the tracer concentration field computed with using Eq.1, the former velocity fields depending on $\boldsymbol{\mu_1}$ and from parametrized inlet tracer concentration $f_{in}$ and diffusion coefficient $D$. The second component of $\boldsymbol{\mu}$ is denoted as $\boldsymbol{\mu_2} = (f_{in}, D, t_i)$ where $t_i$ is the selected time in $[0, T]$. The inlet tracer concentration is sampled regularly between 0.5 and 1.5 $kg/m^3$ and the diffusion coefficient $D$ between $0.001cm^2/s$ and $0.00001cm^2/s$ The choice of the number of basis element for the POD is based on the projection error controlling the quality of the POD approximation. The methodology to check the accuracy of the approximation is detailed in [16]. We have retained $N_V = 2$ elements for each velocity component along $x$,$y$ or $z$ in the stationary case and $N_R = 6 \times 8$ basis functions for the Radon projections. Good reconstruction results can be obtained with this small number of basis elements which is nearly optimal for the simple flow patterns investigated and this choice enables a comparison with the POD-adjoint method.

After this offline stage, in order to train the network, we have generated 800 samples for the velocity field and their paired Radon projections, and we have estimated their POD coefficients. For the test data set, 200 snapshots data have been used for each noise level to obtain Monte-Carlo estimate of the errors. For comparison with POD adjoint based method, 50 samples have been used to estimate the errors with this variational method.

## 3.2 | Neural network architecture and training

In this section, we detail the network architectures and the training method. The training was implemented using the open-source library Keras 2.2.5 with Tensorflow backbone and performed on a modern HPC cluster with 10 processors. Different architectures have been considered for the two POD based netwokrs which are displayed on the schematic Figure 3. For the POD-FC network, the best results have been obtained with a fully connected neural network with 4 internal layers of width (500, 1000, 1000, 1000) between the input and the output with Relu activation function, except in the last layer. For this network architecture, the best results have obtained with a dropout layer after the first layer with a rate of 0.2 to avoid overfitting.

For the POD-CNN network, we use a 3D convolutional architecture to extract the POD coefficients characterizing the reduced dynamics from the Radon projections snapshots input dataset. The 3D CNN operations, filter lengths and strides are summarized in Figure 3. The input to the convolutional layers is a 4D tensor, except for the input layer which is of shape $(N_t, N_\theta, N_z)$. The projection value used for each angle $\theta$ is the average along the $s$ direction. The $L^{th}$ layer takes each 3D slice of the tensor of the layer $L-1$ and convolve them with all the kernels to create a 4D tensor. For any convolutional layer $L$, we denote $k_L$ the number of feature channels. We can group these kernels of size $f_x \times f_y \times f_z$ into a 4D tensor $K^L \in \mathbb{R}^{f_x \times f_y \times f_z \times k_L}$. A schematic drawing together with the shapes $(f_x, f_y, f_z, k_L)$ are presented in Figure 3 We use three convolutional layers with shapes $(f_x, fy, f_z) = (5, 5, 5)$ and strides (2,2,2). The 3D convolutional layers are followed by a feed forward networks with 300 neurons to return a vectorized feature map $(\alpha_j^x)_{1\le j\le N_V} \times (\alpha_j^y)_{1\le j\le N_V} \times (\alpha_j^z)_{1\le j\le N_V}$. Nonlinearities are introduced in the network with RELU activation function. The number of hidden layers, the number of weights per hidden layer, the nonlinear activation functions, the batch size for mini-batch gradient descent, the number of epochs to perform training have been optimized. The network is trained on 100 epochs, with an Adam optimizer, and a decreasing learning rate between $10^{-3}$ and $10^{-4}$. The cost function used is given in Eq.7. We did not used U-net architecture for comparison because several studied have shown that with this architecture , the choice and training of parameters is linked to the grid resolution. The methods used in this work are resolution invariant.

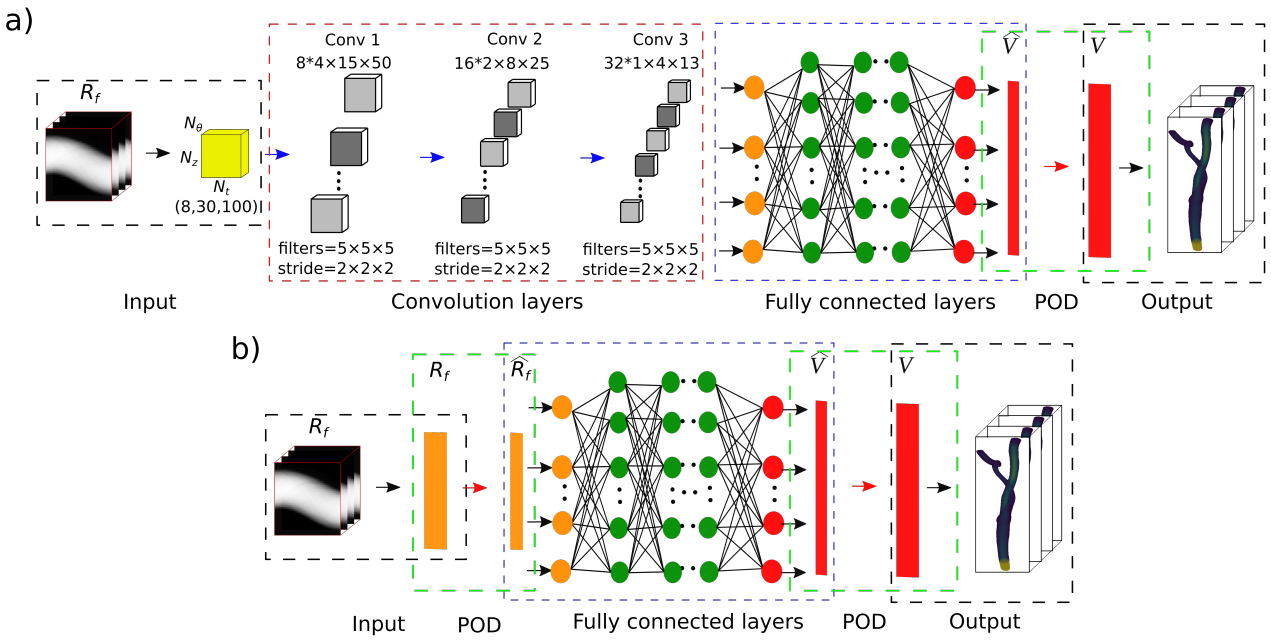


**Figure 3** Architecture of the networks a) POD-CNN network b) POD-FC-POD network.

# 4 | RESULTS AND DISCUSSION

## 4.1 | Results

In this section, we present numerical results and we compare the proposed POD based deep learning methods against the adjoint method. We test the proposed algorithms on stationary velocity fields. We compare the results for different noise levels, visualize the recovered solutions and analyze the accuracy of the reconstruction of the various approaches.

For a qualitative evaluation of the POD-FC method, some examples of reconstruction of the various components of the velocity field is presented on Figure 4 together with the ground truth velocity for a high noise level, for selected simulation times and cross-sections. Results for high and low inlet velocities are displayed in order to show that the methods work for a large range of velocity values. The figure also dislays the error maps for the velocity components. The reconstructions obtained with POD-CNN is rather similar. The error fields of POD-FC and POD-CNN have similar structures, length scales, and error magnitudes, indicating that their output spaces are similar. This figure shows that the approaches based on deep learning leads to good reconstruction results.

In order to evaluate quantitatively the studied coupled POD-deep learning approach, we have compared the reconstructed velocity fields with the ground truth fields based on the normalized root mean square defined by:

$$E(\mathbf{V}) = \frac{\|\mathbf{V} - \mathbf{V}_{true}\|_2}{\|\mathbf{V}\|_2} \tag{12}$$

where $\mathbf{V}$ is the reconstructed velocity and $\mathbf{V}_{true}$ the corresponding true one in the 3D domain. The same normalized error can be claculated for the component along $x$,$y$ and $z$ of the velocity field. We have calculated the meand and the standard deviations for these errors on the test dataset. The Monte-Carlo estimate was evaluated with 200 snapshots for the samples obtained with deep learning. The studied algorithm was evaluated for several noise realizations. The results are summarized in Table 1. The reconstruction times are 35 s and 3.8e-3s and 9.6e-4s for the POD-adjoint, POD-CNN and POD-FC methods respectively for one test sample.

**Table 1** Comparison of the reconstruction errors for the methods POD-FC POD-adjoint and POD-CNN for two noise levels. The mean and standard deviation are given for each method and noise level.

| NMSE | PPSNR(dB) | POD-adjoint | POD-CNN | POD-FC |
|---|---|---|---|---|
| V | 20 | 0.061 (0.042) | 0.025 ( 0.062 ) | 0.01 (0.040) |
| V | 0 | 0.082 (0.061) | 0.024 (0.035) | 0.024 (0.033) |
| $V_x$ | 20 | 0.081 (0.085) | 0.028 (0.045) | 0.014 (0.086) |
| $V_x$ | 0 | 0.096( 0.090) | 0.025 (0.038) | 0.027 (0.038) |
| $V_y$ | 20 | 0.070 (0.075) | 0.029 (0.035) | 0.010 (0.040) |
| $V_y$ | 0 | 0.082 (0.086) | 0.026 (0.032) | 0.029 (0.032) |
| $V_z$ | 20 | 0.051 (0.042) | 0.024 (0.040) | 0.009 (0.060) |
| $V_z$ | 0 | 0.074 (0.062) | 0.022 (0.036) | 0.029 (0.033) |

The CPU time for the generation of one snapshot for the tracer concentration is 700 s and the training of the deep learning models requires 6000 s. Thus the offline CPU time is twice higher for the adjoint method than for the deep learning methods because the evolution with time of the adjoint variable has also to be calculated.

In this work, we consider the $z$ axis is the main flow direction but this choice is arbitrary. In order to show that the method can be applied for complex geometries, we display some reconstructions results near the bifurcation of the vessel and in the curved part of the vessel in Figure 5 and 6. This figures show that the reconstruction errors are small in this regions.

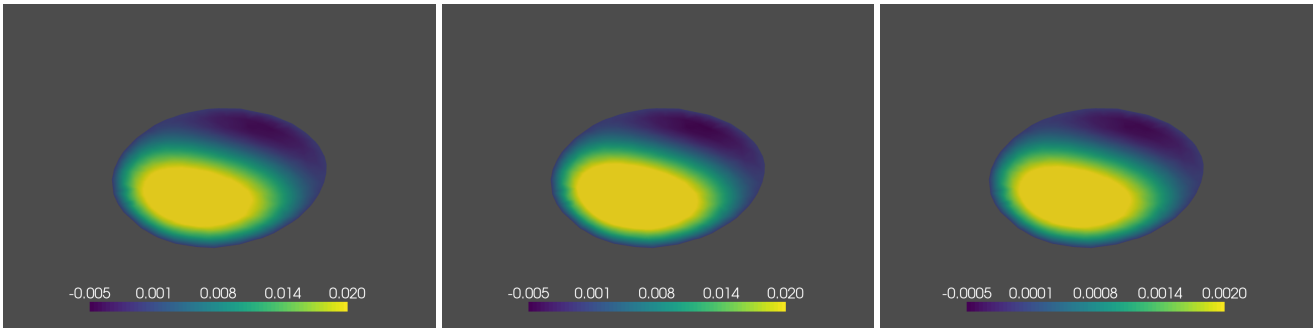


(a) Ground true velocity along x (b) Reconstructed velocity along x (c) Error map for velocity along x

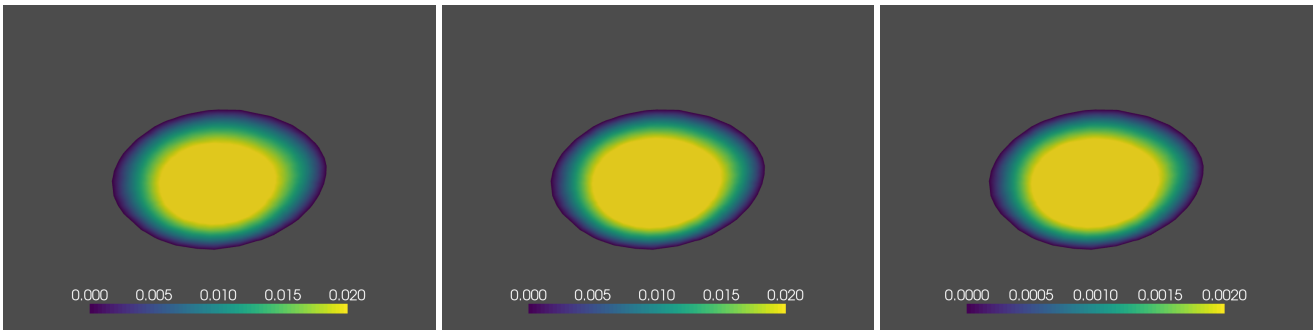


(d) Ground true velocity along y (e) Reconstructed velocity along y (f) Error map for velocity along y

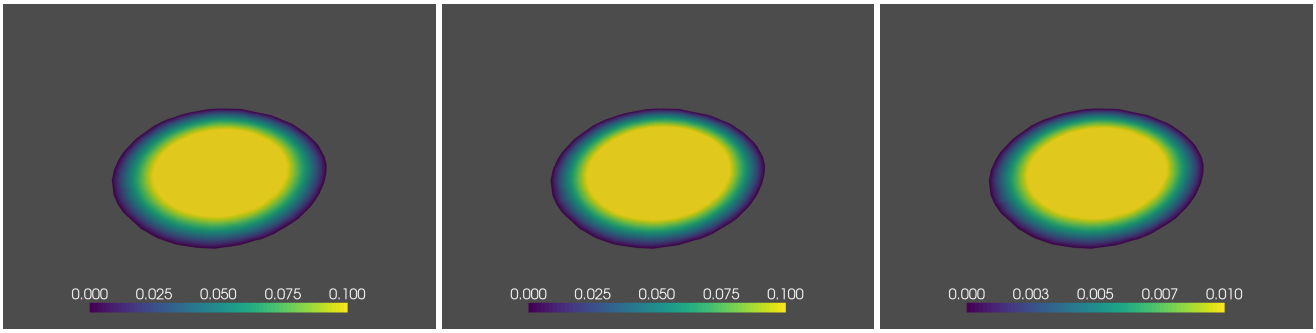


(g) Ground true velocity along z (h) Reconstructed velocity along z (i) Error map for velocity along z

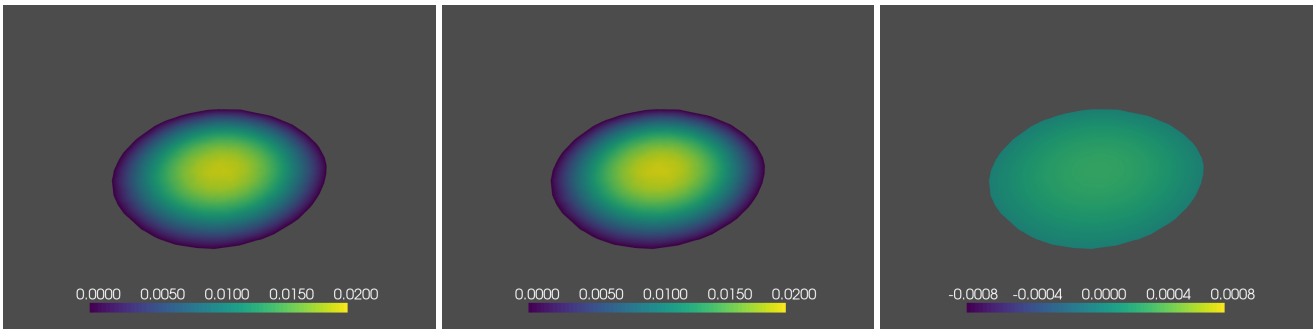


(j) Ground true velocity along z (k) Reconstructed velocity along z (l) Error map for velocity along z

**Figure 4** Example of velocity field reconstruction obtained with POD-DL approach, for the section z=0.155. Figures (a-i )correspond to an inlet velocity 0.5 m/s, outlet pressure 500Pa, inlet tracer concentration 1.1 kg/$m^3$, diffusion coefficient D=1e-5, noise level 0dB. Figures (j-l) correspond to an inlet velocity of 0.025 m/s.

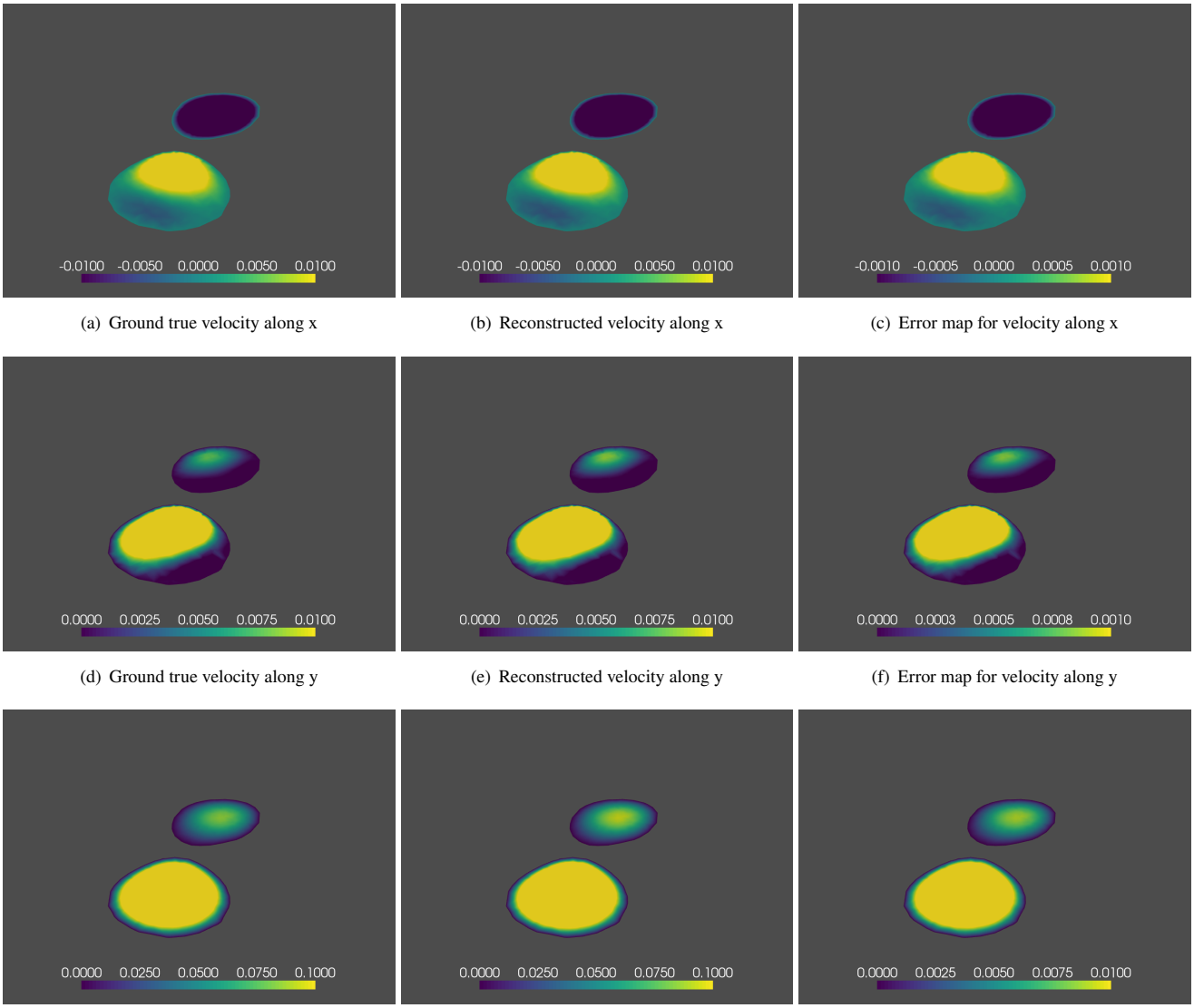


(a) Ground true velocity along x (b) Reconstructed velocity along x (c) Error map for velocity along x

(d) Ground true velocity along y (e) Reconstructed velocity along y (f) Error map for velocity along y

(g) Ground true velocity along z (h) Reconstructed velocity along z (i) Error map for velocity along z

**Figure 5** Example of velocity field reconstruction obtained with POD-DL approach, for the section z=0.165, inlet velocity 0.5 m/s, outlet pressure 500Pa, inlet tracer concentration 1.1 kg/$m^3$, diffusion coefficient D=1e-5, noise level 0dB.

## 4.2 | Discussion

A large number of studies have shown the decisive role of blood flow and disturbed shear stress patterns in clinical atherosclerosis. The studied appoaches achieve a more detailed flow information than classical methods like NMR or ultrasound with a better spatial resolution. The accuracy of the reconstruction of the longitudinal component of the velocity field is improved. In the framework of our simulations, the resolution for the longitudinal component of the velocity can be estimated as the maximum size of the tetrahedra in the mesh. The estimated resolution, 0.1mm, is better than the typical resolution for phase contrast MRI[5]. The developed inversion methods can also estimate accurately the transverse components of the velocity field.

The methods based on a coupling of POD and deep learning significantly outperform the adjoint method for both noise levels. The POD-FC method achieves slightly lower reconstruction errors compared to the approach based on a CNN. The accuracy of the reconstrutions decreases when the noise level increases. In terms of complexity, and simulation times the POD-FC networks is slightly better. For a low noise level, the reconstruction errors are slower for the POD-FC networks compared to the ones of the POD-CNN. These errors are similar for higher noise levels. Good reconstructions results are also obtained for the transverse

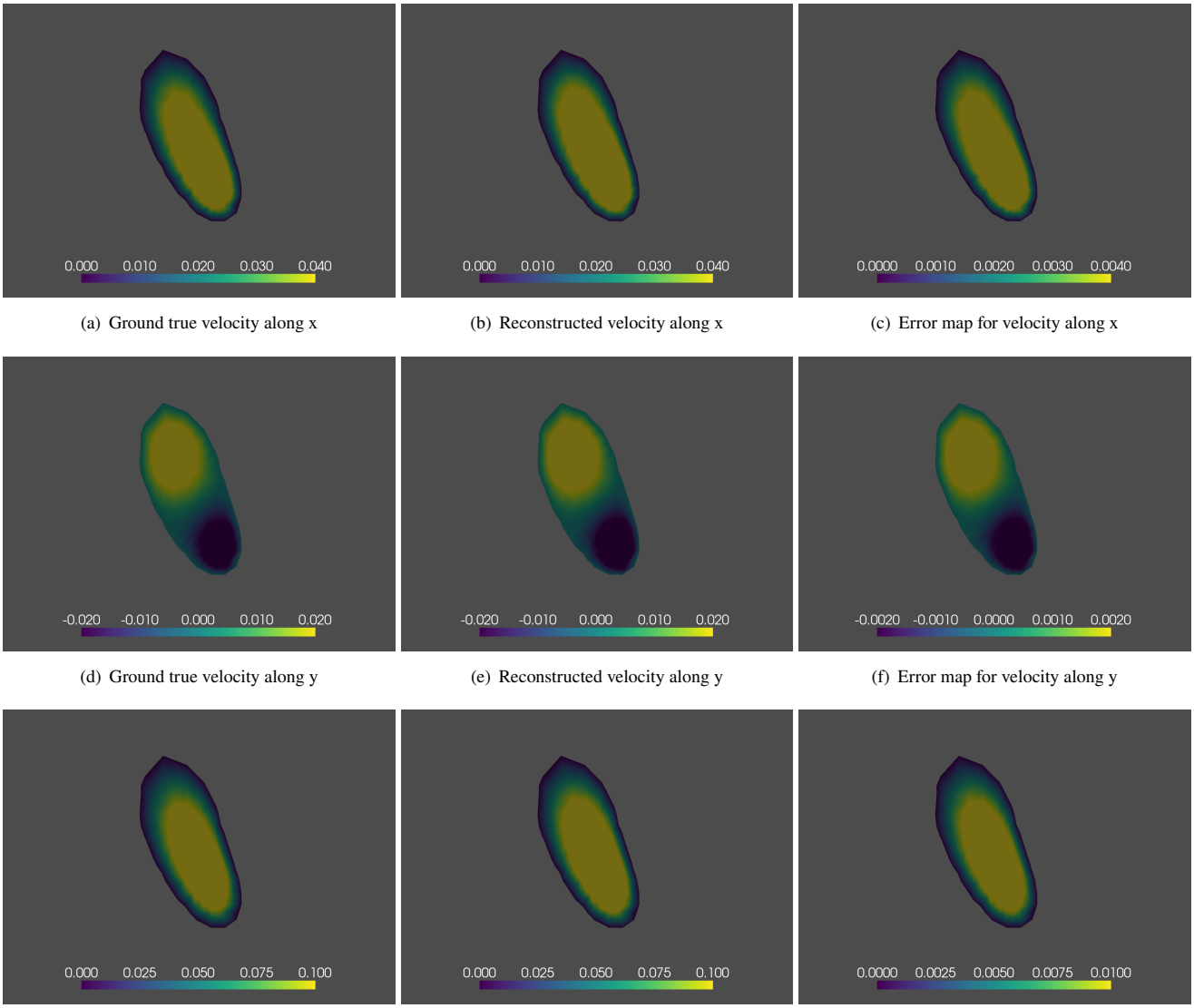


(a) Ground true velocity along x (b) Reconstructed velocity along x (c) Error map for velocity along x

(d) Ground true velocity along y (e) Reconstructed velocity along y (f) Error map for velocity along y

(g) Ground true velocity along z (h) Reconstructed velocity along z (i) Error map for velocity along z

**Figure 6** Example of velocity field reconstruction obtained with POD-DL approach, for the section y=0.144, inlet velocity 0.5 m/s, outlet pressure 500Pa, inlet tracer concentration 1.1 kg/$m^3$, diffusion coefficient D=1e-5, noise level 0dB.

components of the velocity field. The simultaneous reconstruction of the axial and transverse components of the velocity can thus be achieved. When more basis functions are included in the POD approach, the errors stagnates and the basis can be considered as nearly optimal for the inversion for the range of $\boldsymbol{\mu}$ values studied associated to simple flow patterns. All the approaches have a high offline cost since they are based on the calculation of the POD bases. The online runtime of the presented deep learning methods is significantly smaller than the one of the classical variational method and the deep learning methods are practical methods. The small convergence times of the numerical solution can be useful for clinical applications. They are the more suitable approach for applications where the velocity field has to be estimated several times. It makes it a practical method when needing to compute several solutions in parallel.

In this work, we have leveraged some ideas proposed in recent papers for data-driven approximation of nonlinear mappings with model reduction. The models use couplings between reduced bases and deep neural networks. They are examples of physics informed deep learning approaches. The numerical experiments on realistic examples show the effectivenes of the proposed approaches for the solution of our nonlinear dynamic inverse problem and illustrate the interest of deep learning methods for inverse problems wih parametric partial differential equation constraints. They perform well even in the presence of noise. The

POD acts as a physics based regularization. The deep learning techniques investigated can reduce the expensive computational time required for complex biomedical Computational Fluid Dynamics simulations.

The adjoint method based on POD model reduction has the major disadvantage of being intrusive since it requires the knowledge of the system operators and of the governing transport pde during the projection step. In conventional Computational Fluid Dynamics simulations, realistic boundary conditions, initial conditions, and material properties are required. However, determining these conditions is usually challenging and sometimes becomes impossible if the measurement methods are invasive. In this work, we have investigated non-intrusive, purely data-driven reduced order modeling. The methods presented do not require the knowledge of the forward mapping. The deep learning approaches can give accurate reconstruction without the precise knowledge of underlying physics like the intial and boundary conditions for $f$, for $V$ and like the diffusion coefficient $D$ in the transport equation.

We can mention several limitations of the proposed approach and possible directions for future research. We have only considered stationary velocity fields and the method must be extended to more complex non stationary velocity fields with inflow weveforms. Linear projection-based reduced order methods may not be optimal for dimensionality reduction for complex flow patterns because the number of required modes increases significantly. Manifolds for real data are expected to be strongly nonlinear and one needs to make use of nonlinear techniques. Neural network-based autoencoders[37] have been investigated as an alternative for nonlinear approximation because they can address some of the limitations of linear projection techniques. Autoencoders allow to learn nonlinear relations between the input and the output datasets and nonlinear manifolds. They provide a greater flexibility for the dimensionality reduction[38,39,40,41]. Some architectures combining deep learning and reduced order modeling with this type of network have been proposed to improve predictions abilities for 2D flows[42]. The use of autoencoders and nonlinear representations could thus improve the results presented in this work when the methods will be applied to more complex flow patterns. Our geometry is precisely defined and known accurately and no motion of the vessel is taken into account. We have not considered varying domains with fluid-structure interactions. Yet, it will be possible extend the presented approach with geometrical parametrization and with a dimension reduction applied to moving domains and meshes. Autoencoders could provide a great flexibility for the dimensionality reduction for the degrees of freedom corresponding to different types of blood vessel geometry. We have made also the assumption of Newtonian and incompressible fluid flow governed by the Navier-Stokes equations. Whereas blood can be assumed to be a Newtonian fluid in large vessels (especially in most arteries), its viscosity varies with flow rate in smaller arteries and capillaries. For medical conditions such as stenosis, a non-Newtonian model may be preferred over a Newtonian model . Yet, the proposed algorithms can also be used when the underlying physics is non-Newtonian for example with blood flows in small vessels. With the proposed method, we can estimate the velocity of the blood from the Radon projections of the tracer but we can not retrieve the pressure field because we use as regularization the transport equation which only involves the velocity field. This is a drawback of the approach since the pressure field is an important hemodynamic parameter for diagnosis. Yet, it could be interesting to post-process the velocity field to retrieve the pressure field with networks like physics-informed neural networks based on the Navier-Stokes equation.

The presented study uses only synthetically generated data. We intend to apply the approach to real-world cardiovascular data in order to obtain an accurate quantification of the hemodynamics in the vascular networks to improve the clinical diagnosis of vascular diseases. In order to apply the studied approach to real clinical and imaging problems, patient specific vessel models should first be obtained with CT images. A database of several solutions must then be collected by solving the original high fidelity model for different physical and/or geometrical parameters during the offline phase.

## 5 | CONCLUSION

We have developed a new inversion methods to estimate the blood flow from Radon projections perpendicular to a vessel direction. The approaches presented couple POD reductions with deep learning networks. The methods extracts a reduced bases from a collection of high-fidelity solutions via a proper orthogonal decomposition and employs artificial neural networks, fully connected neural networks or convolutional neural networks, to accurately approximate the coefficients of the velocity field to be reconstructed. Numerical results on steady velocity fields confirm the accuracy of the proposed methods and show the substantial speed-up enabled at the online stage as compared to a traditional POD strategy with the adjoint method. The best results are obtained when the POD is performed on the input and output spaces with a fully connected network mapping the coefficients of the decompositions.

## 6 | ACKNOWLEDGMENT

The authors acknowledge financial support of the China Scholarship Council(CSC).

## 7 | CONFLICT OF INTEREST

All the authors declare they have no confict of interest.

## 8 | ETHICAL STATEMENT

None

## References

1. Shi Y, Lawford P, Hose R. Review of zero-d and 1-d models of blood flow in the cardiovascular system. *Biomedical Engineering on line* 2011; 10: 1–38.
2. Crosetto P, Reymond P, Deparis S, Kontaxakis D, Stergiopulos N, Quarteroni A. Fluid-structure interaction simulation of aortic blood flow. *Computers and Fluids* 2011; 43: 46–57.
3. Quarteroni A, Manzoni A, Vergara C. The cardiovascular system: mathematical modeling, numerical algorithms, clinical application. *Acta Numerica* 2017: 1–202.
4. Jiang J, Kokeni P, Magnano C, Zivadinov R, Mark Haacke E. Quantifying errors in flow measurement using phase contrast magnetic resonance imaging: comparison of several boundary detection methods. *Magn.Res.Imaging* 2015; 33: 185–193.
5. Pelc NJ, Sommer FG, Li KCP, Brosnan TJ, Herfkens RJ, Enzmann DR. Quantitative magnetic resonance flow imaging. *J.Magn.Reson.Q* 1994; 10: 125–147.
6. MacDonald ME, Frayne R. Cerebrovascular MRI: a review of state-of-the-art approaches, methods and techniques. *NMR in Biomedicine* 2015; 28: 767–791.
7. Markl M, Schnell S, Wu C, et al. Advanced flow MRI: emerging techniques and applications. *Clinical Radiology* 2016; 71: 779–795.
8. Prevrhal S, Forsythe CH, Harnish RJ, Saeed M, Yeh BM. CT angiographic measurement of vascular blood fowl velocity by using projection data. *Radiology* 2011; 261: 923–929.
9. Korporaal JG, Benz MR, Schindera ST, Flohr TG, Schmidt B. Contrast gradient-based blood velocimetry with computed tomography. *Investigative Radiology* 2016; 51: 1–9.
10. Bouillot P, Brina , Chnafa C, et al. Robust cerebrovascular blood velocity and flow rate estimation form 4D-CTA. *Medical Physics* 2019; 46: 2126–36.
11. Barfett JJ, Velauthapillai N, Fierstra J, et al. Intra-vascular blood velocity and volumetric flow rate calculated from dynamic 4D CT angiography using a time of flight technique. *The International Journal of Cardiovascular Imaging* 2014; 30: 1383–1392.
12. Daly SM, Leahy MJ. Go with the flow: a review of methods and advancements in blood flow imaging. *Journal of Biophotonics* 2013; 6: 217–255.
13. Huang S, Sigovan M, Sixou B. Reconstruction of vascular blood flow in a vessel from tomographic projections. *Biomedical Physics and Engineering Express* 2021; 7: 065032.

14. Herzog M, Kunisch K. Algorithms for PDE-constrained optimization.. *GAMM-Mitteilungen* 2010; 33: 163–176.

15. Plessix RE. A review of the adjoint-state method for computing the gradient of a functional with geophysical applications. *Geophys.J.Int.* 2006; 167: 495–503.

16. Huang M, Sixou B. POD method for acceleration of blood flow reconstruction in a vessel with contrast enhanced X-ray CT. *Computer Methods in Biomechanics and Biomedical Engineering: Imaging & Visualization* 2022.

17. Arridge S, Maass P, Oktem O, Schonlieb C. Solving inverse problems using data-driven models. *Acta Numer.* 2019; 28: 1–174.

18. Rai R, Sahu C. Driven by Data or Derived Through Physics? A Review of Hybrid Physics Guided Machine Learning Techniques With Cyber-Physical System (CPS) Focus. *IEEE Access* 2020; 8: 71050–71073.

19. Karpatne A, Atluri G, Faghmous G, et al. Theory-guided data science: A new paradigm for scientific discovery from data. *IEEE Transactions on Knowledge and Data Engineering* 2017; 10: 2318–2341.

20. Jia X, Willard J, Karpatne A, et al. Physics-guided machine learning for scientific discovery: An application in simulating lake temperature profiles. *ACM/IMS Transactions on Data Science* 2020; 2: 1–26.

21. Raissi M, Perdikaris P, Karniadakkis G. A deep learning framework for solving forward and inverse problems involving nonlinear partial differential equation. *Journal of Computational Physics* 2019; 378: 686–707.

22. Zhu Y, Zabaras N, Koutsourelakis P, Perdikaris P. Physics-constrained deep learning for high-dimensional surrogate modeling and uncertainty quantification without labeled data. *Journal of Computational Physics* 2019; 394: 56–81.

23. Geneva N, Zabaras N. Modeling the dynamics of PDE systems with physics-constrained deep auto-regressive networks. *J Comput Phys* 2020; 403: 109056.

24. Hoop V. dM, Huang D, Qian E, Stuart A. The Cost-Accuracy Trade-Off In Operator Learning With Neural Networks. *Journal of Machine Learning* 2022; 1: 299–341.

25. Bhattacharya K, Hosseini B, Kovachki NB, Stuart AM. Model reduction and neural networks for parametric PDEs. *The SMAI Journal of Computational Mathematics* 2021; 7: 121–157.

26. Lu L, Jin P, Pang G, Zhang Z, Karniadakis G. Learning nonlinear operators via deeponet based on the universal approximation theorem of operators. *Nature Machine Intelligence* 2021; 3: 218–229.

27. Lu L, Meng X, Cai S, et al. A comprehensive and fair comparison of two neural operators (with practical extensions) based on FAIR data. *Comput.Methods Appl.Mech.Eng.* 2021; 393: 14778.

28. Tenderini R, Pagani A, Deparis S. PDE-aware deep learning for inverse problems in cardiac electrophysiology. *SIAM J.Sci.Comput.* 2022; 44: B605-B639.

29. Natterer F. *The Mathematics of Computerized Tomography*. Chichester, UK: Wiley . 1986.

30. Goda K. A multistep technique with implicit difference schemes for calculating two or three dimensional cavity flows. *Journal of Computational Physics* 1979; 30: 76–95.

31. Logg A, Margal KA, Wells GN. Automated solution of differential equations by the finite element method, The Fenics book. In: Lecture Notes in Computational Science and Engineering. 2012.

32. Morton KW, Mayers DF. *Numerical Solution of Partial Differential Equations*. Cambridge, UK: Cambrige University Press . 1994.

33. Hood P, Taylor C. A numerical solution of the Navier-Stokes equations using the finite element technique. *Comp.and Fluids* 1973; 1: 73–100.

34. Glowinski P, Pironneau F. Finite element methods for Navier-Stokes equations. *Annual Review of Fluid Mechanics* 1992; 24: 167–204.

35. Temam R. *Navier-Stokes equations*. Providence, RI: AMS Chelsea Publishing . 2001.

36. Virtanen P, Gommers R, Oliphant T, et al. SciPy: Fundamental algorithms for scientific computing in python.. *Nature methods* 2020; 17: 261–272.

37. Dong G, Liao G, Liu H, Kuang G. A review of the autoencoder and its variants: A comparative perspective from target recognition in synthetic-aperture radar images. *IEEE Geoscience and Remote Sensing Magazine* 2018; 6: 44–68.

38. Gupta R, Jaiman R. Three-dimensional deep learning-based reduced order model for unsteady flow dynamics with variable Reynolds number. *Physics of Fluids* 2021; 34: 033612.

39. Lee K, Carlberg K. Model reduction of dynamical systems on nonlinear manifolds using deep convolutional autoencoders. *Journal of Computational Physics* 2020; 404: 108973.

40. Gonzalez F, Balajewicz M. Deep convolutional recurrent autoencoders for learning low-dimensional feature dynamics of fluid systems. *arXiv preprint arXiv:1808.01346* 2018.

41. Boink Y, Brune C. Learned SVD: solving inverse problems via hybrid autoencoding. *arXiv:1912.10840* 2020.

42. Fresca S, Manzoni A. Real-time simulation of parameter-dependent fluid flows through deep learning-based reduced order models. *Fluids* 2021; 6: 259.